A two-Martian year survey of the water vapor saturation state on Mars based on ACS NIR/TGO occultations

Anna Fedorova (1), Franck Montmessin (2), Alexander Trokhimovskiy (1), Mikhail Luginin (1), Oleg Korablev (1), Juan Alday (3), Denis Belyaev (1), James Holmes (3), Franck Lefevre (2), Kevin Olsen (4), Andrey Patrakeev (1), Alexey Shakun (1)

(1) Space Research Institute (IKI) RAS, Moscow, Russian Federation (fedorova@iki.rssi.ru),

(2) LATMOS/CNRS, Guyancourt, France,

(3) The Open University, Milton Keynes, UK

(4) Department of Physics, University of Oxford, Oxford, UK.

Abstract

On Mars, saturation is the major factor constraining the vertical distribution of water vapor. Recent measurements of water and temperature profiles showed that water can be strongly supersaturated at and above the level where clouds form during aphelion and perihelion seasons. Since 2018, the near-infrared spectrometer (NIR) of the Atmospheric Chemistry Suite onboard the Trace Gas Orbiter has measured H_2O and temperature profiles using solar occultation in the infrared from below 10 km to 100 km of altitude. Here we provide the first long-term monitoring of the water saturation state. The survey spans 2 Martian years from Ls=163° of MY34 to the Ls=180° of MY36. We found that water is often supersaturated above aerosol layers. In the aphelion season, water mixing ratio above 40 km in the mid-to-high latitudes was below 3 ppmv and yet is found to be supersaturated. Around perihelion, water is also supersaturated above 60 km with a mixing ratio of 30-50 ppmv. Stronger saturation is observed during the dusty season in MY35 compared to what was observed in MY34 during the Global Dust Storm and around perihelion. Saturation varied between evening and morning terminators in response to temperature modulation imparted by thermal tides. Although water vapor is more abundant in the evening, colder morning temperatures induce a daily peak of saturation. This dataset establishes a new paradigm for water vapor on Mars, revealing that supersaturation is nearly ubiquitous, particularly during the dust season, thereby promoting water escape on an annual average.

Plain language summary

The rate of water loss from Mars depends on hydrogen, the main product of the H_2O photodissociation escaping from the upper atmosphere. The ability of water to reach high altitudes and to be a direct source of atomic hydrogen is limited by cloud formation, holding water vapor in the lower atmosphere. This process is regulated by temperature and pressure. The condensation starts when

the temperature is cold enough and condensation nuclei (for example, small dust particles) are available. Or it does not, lacking condensation nuclei, their size being too small, or the temperature drops too fast. Then water vapor becomes supersaturated. Recent studies have shown that Martian water vapor is often supersaturated. Here we present the first seasonal cycle of the saturation state from simultaneous measurements of water and temperature during two Martian years by ACS on the Trace Gas Orbiter. Our results show that supersaturation is typical on Mars. It occurs above clouds both in aphelion and perihelion seasons, as well as in the lower polar atmosphere. We demonstrate supersaturation to be an important factor, facilitating the escape of water. Unlike on the Earth, water easily penetrates through the cold trap where clouds form to reach photodissociation altitudes.

Key points

- Long-term observations of H_2O saturation state in the atmosphere of Mars shows the supersaturation is nearly ubiquitous above aerosol layers
- During the dusty season the supersaturation is stronger in MY35 compared to MY34
- More water was found in the evening terminator and stronger supersaturation in the morning terminator

Introduction

The water vapor vertical distribution in the Martian atmosphere is driven by microphysics, radiative transfer, dynamics and chemistry. Temperature is one of main parameters controlling the saturation of water, which governs cloud formation, and subsequently the vertical distribution of water. Because clouds have a radiative effect (see e.g., Navarro et al., 2014), they generate in turn a feedback loop that impacts climate overall. The cold aphelion season is characterized by a low hygropause that produces clouds and blocks water vapor below 10–20 km, thereby regulating the advection of water from the Northern to Southern Hemisphere (Clancy et al., 1996; Montmessin et al., 2004). In the warm dusty perihelion season, higher atmospheric temperatures induce higher hygropause, with water vapor extending up to 60–80 km (Clancy et al., 1996; Montmessin et al., 2004; Trokhimovskiy et al., 2015a; Fedorova et al., 2021). Recent observations found out that global dust storms have a strong impact on the water vertical distribution. During these events, water can reach up to 100 km, as was observed during the MY28 Global Dust Storm (GDS) (Fedorova et al., 2018; Heavens et al., 2018) and MY34 (Aoki et al., 2019; Fedorova et al., 2020, 2021, Belyaev et al., 2021). Such events constitute a quasi-direct source of hydrogen in the upper atmosphere, accelerating the escape of hydrogen to space (Clarke, 2014; Chaffin et al., 2014, 2017; Krasnopolsky, 2019; Shaposhnikov et al., 2019). In situ sampling by the Mars Atmosphere and Volatile EvolutioN (MAVEN) Neutral Gas and Ions Mass Spectrometer (NGIMS) even showed that water molecules were propelled up to an altitude of 150 km (Stone et al., 2020), producing one of the most spectacular illustration of the tight and fast coupling

between the lower and the upper atmosphere. The link between dust and hydrogen escape has been explored thanks to simultaneous measurements of dust, temperature, ice, water and hydrogen during the regional C-storm of MY34 (Ls 310 and 320°). This isolated dust event boosted planetary H loss by a factor of 5 to 10 (Chaffin et al., 2021). Highly sensitive Trace Gas Orbiter (TGO) measurements were able to profile water up to 120 km during perihelion in MY34 and MY35, and during the MY34 GDS (Belyaev et al., 2021). Together with the multi-annual SPectroscopy for the Investigation of the Characteristics of the Atmosphere of Mars (SPICAM) survey of H_2O vertical distribution (Fedorova et al., 2021), such kind of dataset has proven insightful to address the contribution of the dusty perihelion season and that of the MY34 GDS in enhancing the production of H atoms that eventually make their way to the upper atmosphere (Belyaev et al.,2021).

Supersaturation reflects the ability that water has to penetrate the cold trap associated with cloud formation and propagate above it. It also reveals inefficient condensation process, that may be attributed to a lack of condensation nuclei (CN) or higher resistance to diffusive growth. The first evidence of supersaturated water vapor in the Martian atmosphere was produced by SPICAM on Mars Express. Maltagliati et al. (2011) observed supersaturation reaching 2 to 10 at 30–40 km in the aphelion season, from Ls=50° to 120° in both hemispheres using SPICAM water profiles and collocated Mars Climate Sounder (MCS) temperatures corrected for local time. The observed supersaturated state was then explained by a possible lack of CN due to the scavenging effect; that is, a cleaning of the atmosphere of dust captured by forming ice particles and then dragged to lower altitudes by sedimentation. Yet, Fedorova et al. (2014), analyzing the same set of observations have shown that aerosols, and thus CN, was present in the atmosphere for latitudes below 60N at 30-50 km but mostly with submicron particle size <0.1 µm. Author estimated that the critical saturation ratio for such particles can vary from 2 to 4 for low temperatures of the middle atmosphere that is roughly consistent with Maltagliati et al. (2011). Clancy et al. (2017) used 1.27 µm $O_2(^1\Delta_g)$ dayglow profiles from the Compact Reconnaissance Imaging Spectrometer for Mars (CRISM) limb observations and the Laboratoire de Météorologie Dynamique (LMD) Mars Global Climate Model (GCM) to constrain water profiles and estimate a saturation ratio for Ls=60–140° and 200–310° seasons. A high (>2.2) saturation ratio was found in northern mid-to-high latitudes at 20-40 km, in rough agreement with SPICAM findings. In contrast, Clancy et al. (2017) reported no supersaturation in the southern summer season, when SPICAM found supersaturation of 2–3 times at 80 km in presence of clouds (Maltagliati et al., 2013).

However, these earlier discoveries of supersaturation had to rely on separate temperature estimates and the first simultaneous water vapor and temperature profiles were produced by TGO and ACS (Korablev et al., 2018; Fedorova et al., 2020) experiment dedicated to occultation measurements and vertical profiling of atmosphere. TGO began its science phase in march 2018 of 2018 (L_s=163° of MY34) shortly before the GDS. ACS observed the saturation state on the

global scale during the dusty season and definitely showed that supersaturation occurs even when clouds are present. The supersaturation was detected in both hemispheres above 60–80 km from Ls=210 to 340° and in high latitudes in the lower atmosphere, below 20–30 km.

Poncin et al. (2022) have investigated water vapor saturation in the presence or proximity of water ice clouds for co-located observations of temperature and ice clouds by MCS and water vapor profiles by CRISM and Nadir and Occultation for MArs Discovery (NOMAD) on TGO at various times during the Martian year. During the aphelion season, water was close to saturation in the presence of clouds with supersaturation of 2-3 at the top of the cloud layer. During the perihelion season, the supersaturation up to 1.5 was observed in high southern latitudes near the top of the clouds. Measurements during the GDS of 2018 suggest that supersaturation did not exceed 5. Based on these measurements, a schematic model of cloud evolution was proposed (Poncin et al., 2022) with small particles formed rapidly in supersaturated regions and then growing and falling explaining why water ice was observed even in the subsaturated region below.

Water ice clouds play a key role in the radiative transfer of the Martian atmosphere, impacting its circulation and thermal structure (Madeleine et al., 2012). Therefore, detailed cloud microphysics has become an important component of Mars' Global Climate models (Montmessin et al., 2004, Navarro et al., 2014; Shaposhnikov et al., 2019; 2022). The first time supersaturation was simulated by a climate model, it had to include a cloud microphysics module accounting for nucleation of dust particles, water ice particle growth/sublimation, and scavenging (Navarro et al., 2014). The model found reasonable agreement with SPICAM observations with regard to the supersaturation level predicted above the hygropause. At Ls=210°-240° and 330°-360° studied by authors, temperature clearly controlled the boundary of supersaturation and its values reached 1000 in some cases but the absolute value of water mixing ratio in this region was less than 1 ppmv and negligible compared to total water.

Following TGO observations, Holmes et al., (2021a) studied global variations of water vapor and saturation state in the dusty season of MY34 including the GDS. Using the cloud model of Navarro et al. (2014), they assimilated observed temperature and water fields from a variety of instruments in Mars' climate model. Discrete layers of supersaturated water were found at all latitudes during the dusty season of MY34. They found evidence of water supersaturation above 60 km for most of the GDS period. The GDS and the southern summer regional C- storm (Ls from 310° to 320°) forced water to be supersaturated at altitudes where it can break up and then produce hydrogen atoms that eventually escape to space. The model reanalysis indicates that it happens at all latitudes where ACS observed.

Compared to Fedorova et al. (2020), we present here the full set water vapor saturation state obtained by Near-InfraRed (NIR) ACS spectrometer throughout two Martian years from Ls=163° of MY34 to Ls=170° of MY36, while Fedorova

et al. (2020) stopped their analysis at Ls = 355° of MY34. Since this first publication, the calibration of the instrument and the retrieval procedure and pipeline have been improved as described in Section 2 where an overview of the ACS NIR spectrometer, retrievals and observation coverage are presented as well as observations of H_2O clouds with mid-infrared channel of ACS. Section 3 provides an overview of results focusing on the seasonal, latitudinal, local time and interannual variations. Section 4 discusses the correlation with previous measurements.

2. Observations

2.1 ACS NIR spectrometer

TGO was launched in March 2016 and was inserted into Mars' orbit in October 2016. Routine science began in April 2018 after 18 months of aerobraking that formed a circular 400-km orbit. ACS is a set of three high-resolution spectrometers, Near-InfraRed (NIR), Mid-InfraRed (MIR), Thermal InfraRed (TIRVIM), operating in the spectral range from 0.65 to 17 m onboard the TGO mission.

The NIR spectrometer combines an acousto-optical tunable filter (AOTF), used as a monochromator that can be commanded to isolate a specific wavelength bandpass whose width corresponds to the free spectral range of the echelle grating that operates at high diffraction orders. It covers the 0.7–1.7 µm spectral range using diffraction orders 101 through 49 with high resolving power of about 28000 (Trokhimovskiy et al., 2015b; Korablev et al., 2018). During an occultation, ACS NIR measures ten pre-selected diffraction orders every 2 s. Extremely high spectral resolution allows ACS NIR to sound different atmospheric constituents as H_2O, CO, CO_2, and weak band of O_2 (Korablev et al., 2018; Fedorova et al., 2020; 2021; 2022). The instantaneous FOV of NIR in the direction perpendicular to the limb is small (~0.02°) and limited by the slit width. The instantaneous FOV (IFOV) corresponds to a vertical resolution of 500–600 m at the tangent altitude of the line of sight. The time to measure one diffraction order is 0.2 s, yielding an effective vertical resolution better than 1 km for each diffraction order. The number of detector lines measured in a single occultation and its position on the detector depends on the pointing direction (NOMAD or ACS MIR-driven) and the available downlink volume. It varies from 6 to 30 lines; the solar image size on the detector limits the upper boundary. Averaging 30 detector lines does not worsen vertical resolution, since that dimension of FOV is oriented along the limb. The SNR for an individual pixel and pure solar signal in the AOTF maximum is ~600 for the MIR pointing and ~300 for the NOMAD pointing.

The calibration of the ACS NIR from laboratory measurements and first in-flight data are summarized in Trokhimovskiy et al., 2015a; (Korablev et al., 2018). It included the AOTF characterization dependence to temperature and spectral range, signal-to-noise ratio estimations, blaze function and instrumental line shape and resolving power variation with diffraction order and detector position.

These calibrations were used in the retrievals of temperature and water vapor by Fedorova et al. (2020). The present study includes just one update, an improved characterization of the AOTF profile within the diffraction order 49 to better describe the order overlapping from far sidelobes. The AOTF profile at ~1.565–1.58 µm, close to the long-wavelength bound of the detector, has not been characterized in the laboratory accurately enough and was improved using in-flight solar spectra.

The data processing of ACS NIR in occultation mode was described in Fedorova et al. (2020). The transmittance was obtained as a ratio of spectra measured inside the atmosphere to reference solar spectrum that is averaged spectra outside the atmosphere (above 140-150 km) for each detector line separately. We averaged 6–25 lines inside the solar disc with the maximal signal, excluding the solar image edges, resulting in an SNR of 800–3000, depending on the occultation. Another major improvement compared to previous retrievals, the geometry of the observations was calculated with the latest version of the attitude kernels. The TGO onboard clock was recently found to have a gradually increasing shift with respect to the Universal Time Coordinated (UTC), up to several seconds at maximum, but used here geometry has correction of this anomaly.

2.2 Retrieval algorithm

For this study, we use measurements of diffraction order 49 (6318–6387 cm^{-1}), order 54 (6960–7040 cm^{-1}) and diffraction order 56 (7217-7300 cm^{-1}) (Fig.1A-D). Order 49 was initially used to retrieve the temperature and CO_2 density using the 1.57 m CO_2 band and CO mixing ratio using a weaker overlapping band (Fedorova et al., 2020) (Fig.1B). Order 56 contains the strongest lines of the 1.38 m water vapor band (Fig.5D). Order 54, firstly used here for NIR analysis, contains the strongest (in the NIR spectral range) the 1.43 m CO_2 band. Together with order 49 it was used to retrieve the temperature and CO_2 density especially at altitudes above 80 km where the 1.57 m CO_2 band is weaker.

The retrieval follows the same methodology as the previous temperature and water vapor retrieval with this instrument (Fedorova et al., 2020). A forward model of transmission is computed using a look-up-table of absorption cross-sections (as a function of pressure and temperature) for a corresponding number of atmospheric layers (40 to 130 depending on orbit), using the spectral line parameters from HITRAN 2016 (Gordon et al., 2017) with a correction coefficient of 1.7 for the H_2O broadening in CO_2-dominated atmosphere, as suggested by Gamache et al. (1995) and self-broadening in the case of CO_2.

The first step is a retrieval of temperature and pressure profiles and the CO mixing ratio based from order 49 and separately from order 54. The retrieval is performed using a Levenberg–Marquardt iterative scheme with Tikhonov regularization applied, customary for vertical inversions in order to smooth the profile and minimize the errors. To constrain simultaneous retrieval of temperature and pressure, we assume hydrostatic equilibrium as described in Fedorova

et al. (2020). Results are presented in Figure 1 for temperature (5E) and density (5F) profiles. Both orders have shown very close results and to minimize the uncertainties for future study we use the weight averaged profiles between two orders.

In the next step, the H_2O number density and v.m.r. are retrieved, applying a similar retrieval procedure to the spectra in the diffraction order 56 (7217–7302 cm^{-1}). Only one free parameter vector is retrieved (the H_2O *vmr*) with the pressure and temperature profiles obtained in the previous step. The self-consistent retrieval of the H_2O profile, along with that of CO_2 and the temperature profile, is a more reliable approach than using Climate model predictions of temperature. These predictions are shown to have a bias compared to observations (as shown in Fedorova et al. 2020). Figure 1 (B,C,D) shows the example of spectra with the best-fit synthetic spectra demonstrating the good quality of the data.

The uncertainty on the retrieved quantities is given by the covariance matrix of the solution. In case of water vapor, we account for the Jacobian errors due to the uncertainties in the retrieved T and P. For further analysis, we removed all data with H_2O uncertainties exceeding 100% or with temperature error exceeding 12 K.

ACS NIR measured CO_2 and H_2O vertical profiles together with several instruments onboard TGO. The validation of NIR temperature profiles against ACS MIR results obtained from the 2.7 m band showed a good agreement for a wide set of simultaneous measurements (Alday et al., 2019; 2021; Fedorova et al., 2020; Belyaev et al., 2021). The water profiles were validated with the ACS MIR measurements in 2.6 m water band (Alday et al., 2021; Belyaev et al., 2021).

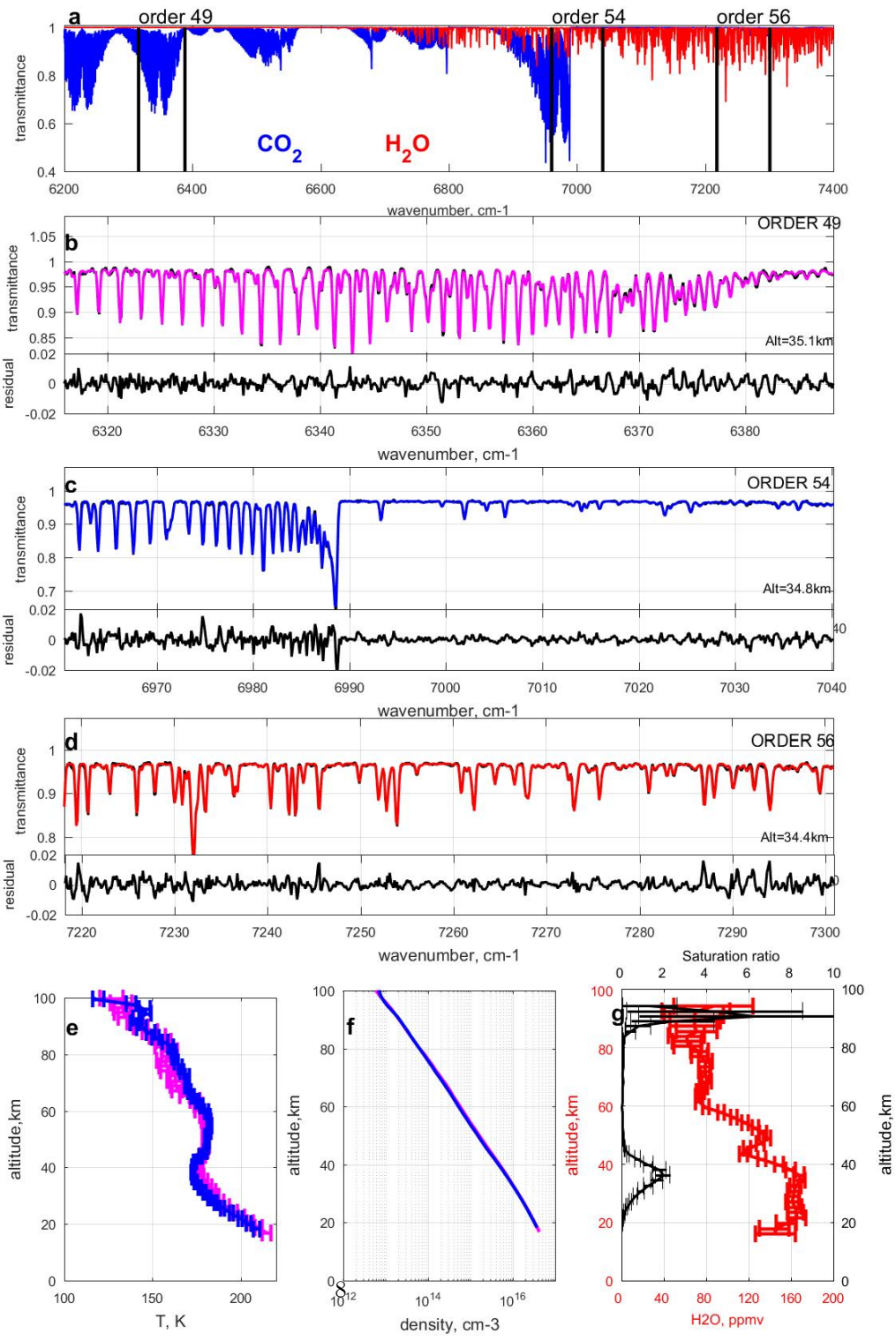
a
order 49
order 54
order 56
transmittance
CO2
H2O
wavenumber, cm-1
b
ORDER 49
Alt=35.1km
residual
c
ORDER 54
Alt=34.8km
d
ORDER 56
Alt=34.4km
e
altitude,km
T, K
f
density, cm-3
Saturation ratio
g
H2O, ppmv

Figure 1. Example occultation spectra of CO_2 and H_2O bands measured by ACS NIR and the retrieved profiles for occultation 4154 in MY34 (Ls=278°, latitude:55°S, longitude 317°E, local time 3:06). A) synthetic spectra of CO_2 and H_2O absorptions (target altitude of 20 km); the ranges corresponding to measured diffraction orders are marked by vertical bars. B) observed (black) and best fit model (magenta) transmittances in order 49 at 35 km with residual. C) observed (black) and best fit model (blue) transmittances in order 54 at 35 km with residual. D) observed (black) and best fit model (red) transmittances in order 56 at 35 km with residual. Lower panels show profiles retrieved from this occultation: (E) temperature in Kelvin from order 49 (magenta) and 54 (blue), (F) CO_2 density in cm^{-3} from the same orders and (G) water vapor mixing ratio in ppmv from order 56 with saturation ratio (black) calculated as explained in Section 2.3.

2.3 Saturation ratio

The water vapor saturation pressure depends solely on temperature in the approximation of the Clausius-Clapeyron (List, 1984), which is applicable to planetary atmospheres. For the computation of the water saturation in the Martian atmosphere, we use a semi-empirical form of the Clausius-Clapeyron law, the Goff-Gratch equation (Goff and Gratch, 1946), that yields the vapor pressure over ice :

$$\log P_{\mathrm{sat}} = 2.07023 - 0.00320991\ T - 2484.896\ T^{-1} + 3.56654 \log T,$$

where P_{sat} is the saturation vapor pressure in mbar and T is the temperature in kelvin.

The saturation ratio S is defined as $S{=}P_{H2O}/P_{sat}$. The uncertainties of S are evaluated as the total differential of S, using the uncertainties of the retrieved temperature, pressure and the water *vmr*.

2.4 Aerosol loading estimation

To complete the water vapor and temperature profiles extraction, the aerosol extinction can also be retrieved. ACS NIR measures the atmospheric extinction in all diffraction orders used during an occultation. Several orders are dedicated to measure aerosol: 78 around 0.99 m (10,052–10,170 cm^{-1}) and order 90 around 0.86 m (11,500–11,734 cm^{-1}). When measuring CO_2 and H_2O using orders 49, 54 and 56, aerosols can be retrieved from the continuum located between the gaseous absorption bands. The NIR extinctions cannot distinguish between dust and water ice aerosol, thus both clouds and dust are mixed into a "generic" aerosol.

To distinguish water ice clouds particles, in addition to NIR we also use aerosol extinction retrieved from ACS MIR occultation data a proxy for aerosol mass loading estimation. This procedure has been described in detail and validated in Fedorova et al. (2020) and the related Supplementary Material.

First, we apply a standard "onion peeling" method (Rodgers, 2000) to re-

trieve vertical profiles of aerosol extinction and associated uncertainties from the ACS solar occultation data for NIR and MIR independently (Fedorova et al., 2009; 2014; 2020). From NIR data, extinction is retrieved from orders 49 (6318–6387 cm^{-1}), 56 (7217-7300 cm^{-1}), 78 (10,052–10,170 cm^{-1}), 90 (11,500–11,734 cm^{-1}), and 101 (13,016–13,170 cm^{-1}), following Luginin et al. (2020). From MIR data, we use spectra measured in the secondary grating position 12 (2905−3265 cm^{-1}), which includes water ice absorption band at 3 m (Fedorova et al., 2020; Stcherbinine et al., 2020).

MIR aerosol extinction at the center of the water ice band (3225 cm^{-1}) is treated as a substitute for "generic" aerosol extinction, and extinction at several other wavelengths allows distinguishing between water ice and dust particles. Specifically, the ratio between MIR extinction at 3225 cm^{-1} and NIR extinction at 10126 cm^{-1} is used to estimate particle size, while the ratio between MIR extinctions at the center (3225 cm^{-1}) and the wing (2922 cm^{-1}) of the water ice band defines the aerosol type (for more details, readers are referred to table S2 in the Supplementary Material of Fedorova et al., 2020). In this work, we use MIR aerosol extinction at 3225 cm^{-1}, which was attributed to water ice, as a proxy to water ice mass loading.

From April 2018 to January 2022, ACS MIR has performed 866 solar occultation measurements in the secondary grating position 12, almost ten times less frequent compared to the NIR channel. Figure 2 shows comparison of MIR extinction at 3225 cm^{-1}, produced by water ice particles with blue color shown the part of extinction satisfying water ice criteria, with one of NIR extinction at 1.4 m for two example observations: 5987_E at L_S 2° of MY 35 at low latitudes, and 12756_I at L_S 289° of MY 35 at high latitudes. To validate the extinction relation method, Figure 2 also contains water ice mass loading retrieved from a complex solution of the inverse problem from the simultaneously recorded MIR and NIR spectra with a procedure, described in Luginin et al. (2020).

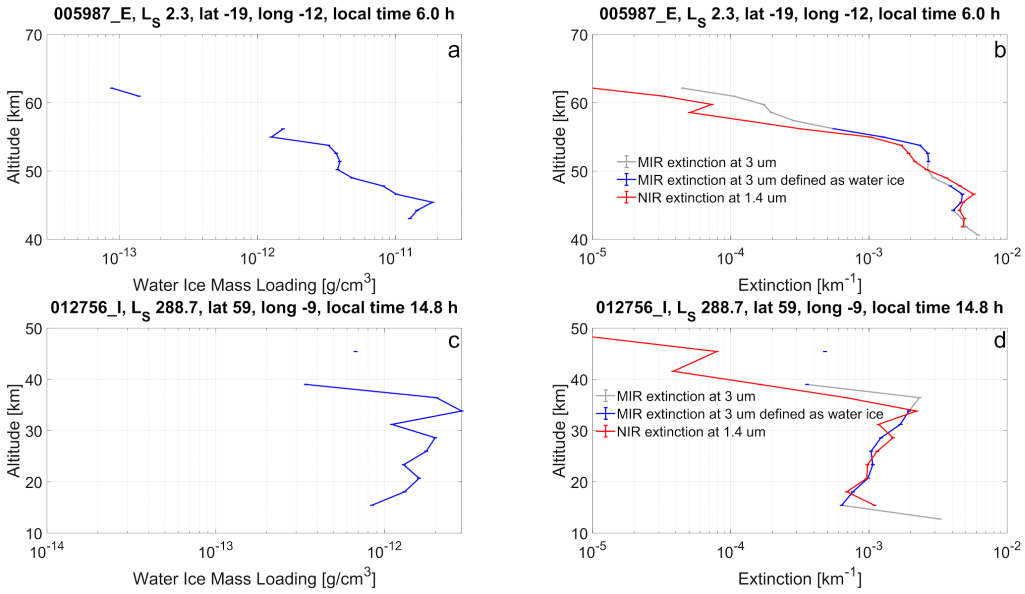

Figure 2. Aerosol loading estimation for observation 5987_E at L_S 2° of MY 35 (top panels), and 12756_I at L_S 289° of MY 35 (bottom panels). Retrieved water ice mass loading (a, c); MIR aerosol extinction at 3225 cm^{-1}, which was attributed to water ice (blue lines at b, d); NIR aerosol extinction at 1.4 m (red lines at b, d). Gray lines at b, d correspond to MIR aerosol extinction at 3225 cm^{-1}, not attributed to water ice particles.

2.5 Dataset

TGO performs an occultation on each node of the 2-h orbit with one or both of two instruments: ACS and NOMAD (Nadir and Occultation for Mars Discovery). Because of a subtle misalignment of the ACS and NOMAD lines-of-sight (LOS), two occultation observing modes are implemented: ACS MIR-driven and NOMAD-driven. ACS NIR operates both kinds of pointing, but ACS MIR can be used only with the ACS pointing. On average, ACS NIR accomplished seven occultations per sol in both hemispheres (from 1 to 21), except during several periods of about 15 to 20 days long without occultations due to orbital plane orientation. ACS NIR provides water vapor in the 1.38 µm band and temperature measurements in 1.57 µm and 1.43 µm CO_2 bands, as well as aerosol extinctions at various wavelengths for each occultation. We analyzed NIR occultation profiles obtained both with ACS and NOMAD pointings (the latter constituting ~40% of profiles). From the beginning of the TGO science phase in April 2018 (Ls=163° of MY34) to January 2022 (Ls=170° of MY36), ACS NIR collected ~8 500 profiles (Figure 3).

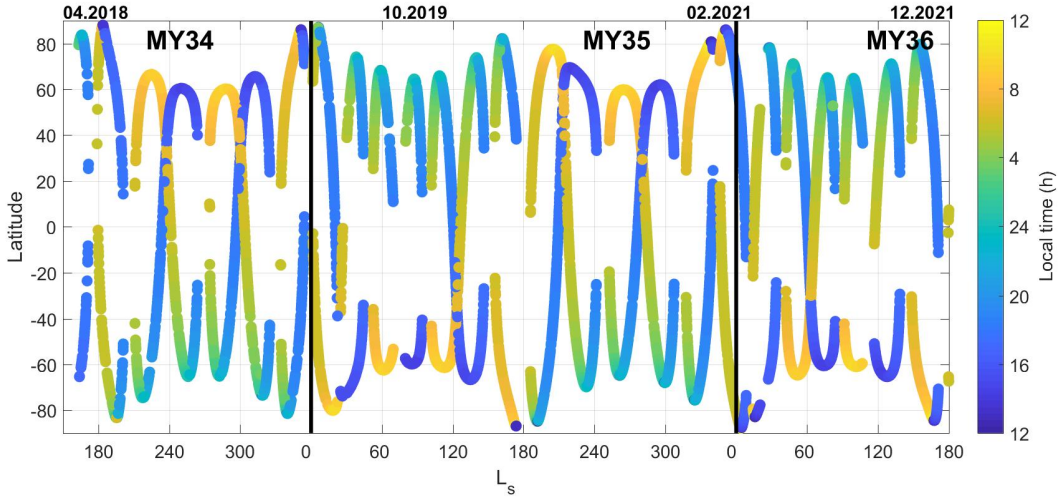

Figure 3. Observational coverage of ACS NIR solar occultations for MY34-36 from April 2018 to January 2022. Colors indicate the local time of the occultation.

3. Results

3.1 Seasonal variations

Figures 4 and 5 show the seasonal variations of temperature, water vapor and saturation ratio in both hemispheres, extracted from our dataset. The map exhibits the well-known imprint of seasons on temperature and water that far exceeds variations due to latitudinal sampling. The first strong increase of water vapor in the atmosphere corresponds to the global dust storm of 2018 that begun shortly after Ls=193° and which was studied in detail in (Aoki et al., 2019, Fedorova et al., 2020, Belyaev et al., 2021). Both hemispheres show a sharp temperature rise of up to 220 K below 60 km (Fig.4B, 5B). The water mixing ratio in the northern hemisphere exceeds 100 ppmv below 80 km and stays at 50 ppmv up to 100 km (Fig.4C). Such a strong increase in water was never observed again after in MY34 and later during the entire MY35. The second strong increase in water at high altitudes corresponds to Ls=240°-300° and is related to perihelion near southern summer solstice when the Hadley circulation cell brings water from the wetter Southern Hemisphere to the Northern Hemisphere (Houben et al., 1997; Richardson and Wilson, 2002a, 2002b; Montmessin et al., 2007). At that season, southern water exceeds 50 ppmv at all altitudes below 100 km and 200 ppmv below 60 km. In contrast, in the Northern Hemisphere two layers of water were observed: (1) a lower layer containing more than 100 ppmv from the lowest observable altitude up to 40-50 km followed by a sharp decrease to 10-20 ppmv between 50 and 70 km, (2) a higher layer marked by an increase up to 30-50 ppmv from 70 to >90 km. This water layer observed both in MY34 and 35 in the upper atmosphere illustrates the strength of water

transport during that part of the year.

A regional "C-storm" occurred in MY34 between L_s 315° and 330°. This type of dust event was studied in detail, combining observations and model to illuminate the water escape in these particular climatic conditions (Stone et al., 2020; Chaffin et al., 2021; Holmes et al., 2021b). The intensity of this event varies from year to year (Kass et al., 2016). Another C-storm in ACS data occurred in MY35 although a little earlier (~10°) in the season where water in the Southern Hemisphere was carried up to 80 km.

Around aphelion, the equatorial region meets its coldest time, leading to a strong decrease of the hygropause and water lines were not observed above 60 km. In the Northern Hemisphere, a water maximum of 200 ppmv was observed below 20-30 km, with hygropause altitude growing from high to low latitudes. Above these altitudes, water sharply decreases down to 1-5 ppmv, which was observed both in MY35 and in MY36 and was well correlated with the decrease in temperature from 200 to 160K (fig.4B,C). In the Southern Hemisphere, water vapor was also observed up to 60 km, but the typical values rarely exceeded 1-3 ppmv except close to the equator where values were found to reach 20 ppm (fig.5C). At that season (Ls=30° to 150°) in the middle latitudes, the atmosphere near 30-40 km is characterized by a warm layer associated with a water abundance of 3-5 ppm. This layer is produced by transport from the Northern Hemisphere. In the cold low atmosphere the temperature does not exceed 160 K and water remains mostly below 1 ppm. Yet water lines are still visible , and a high supersaturation was confidently inferred.

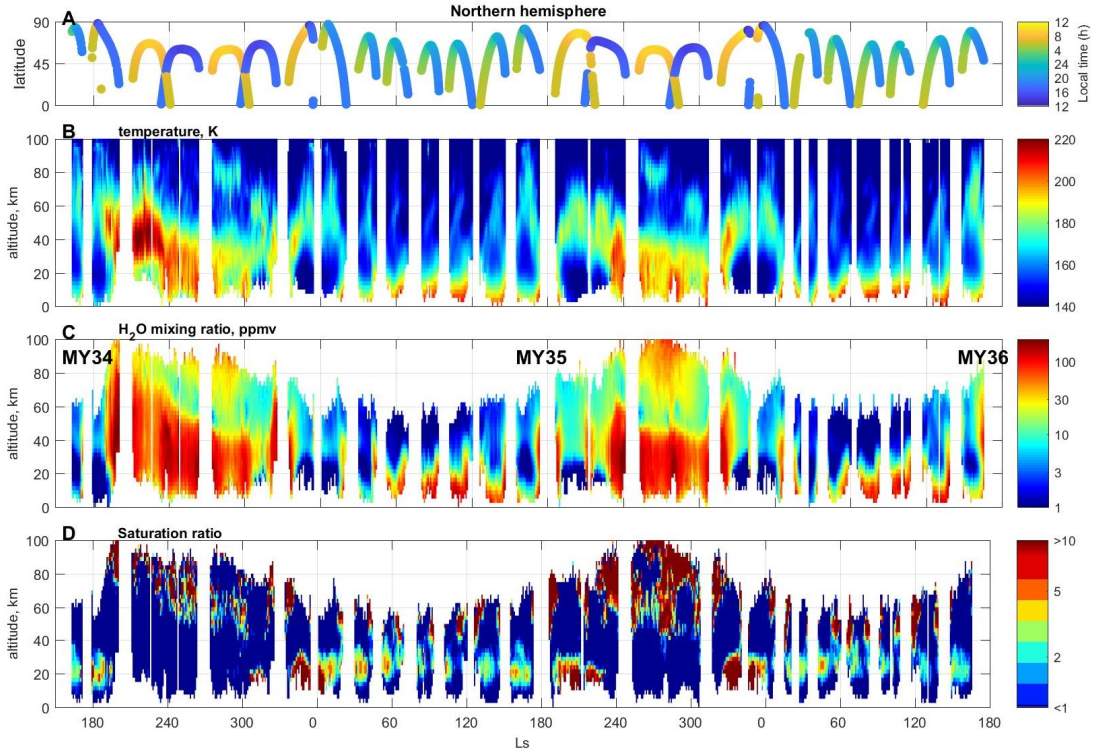

Figure 4. Seasonal variation of temperature (B), water vapor (C) and saturation ratio (D) profiles from Ls=163° of MY34 to Ls=170° of MY36 retrieved from the ACS NIR data in the northern hemisphere. The retrieval was binned into intervals of 1° of L_s and 2 km of altitude. The top panel shows the latitudes and local time of the measurements.

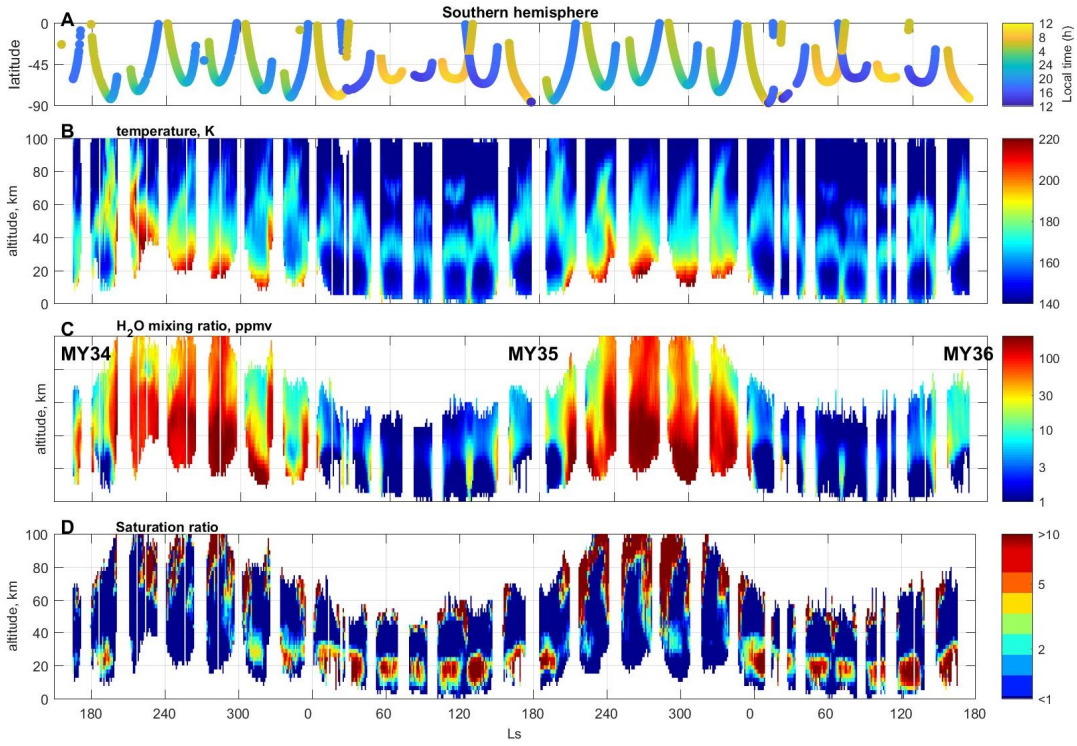

Figure 5. Same as Figure 4, except for the Southern Hemisphere.

3.2 Aphelion season

Figure 6 presents the latitudinal variations of temperature, water vapor, saturation ratio, aerosols, and H_2O ice extinction from Ls=0° to 180° for MY35 and MY36. Shortly after the northern vernal equinox (Ls=0°-30°), temperature, and water are distributed almost symmetrically about the equator, with a warm region of 180K between 30°S to 40°N from the surface up to 40 km (Fig.6A). The picture is very close for both years, despite the difference in latitude coverage. In the mid-to-high latitudes, warm layers of about 180 K were observed in both hemispheres at 40-60 km with temperature minima near the poles at low altitudes named "polar vortex" (Heavens et al., 2011). Water vapor also shows a maximum at 40 km with a mixing ratio of 50 ppmv between 30°S to 40°N, which then sharply decreases to 3-5 ppmv between 40 and 60 km (Fig. 6B). In the mid-latitudes, the prominent 10 ppmv branch of water at 40-60 km that is visible in both years is a consequence of the transport of water from the equatorial region to high latitudes. Below 20 km poleward of 60° in both hemispheres, water abundances decrease abruptly to the sub-ppm level. Downwelling water starts to be strongly supersaturated (fig.6C) with clouds' formation (fig.6D) in

this polar region in MY35 and MY36 in the South and only in MY35 in the North . In the North, saturation ratios of only <3 were detected. The difference in this region between MY35 and 36 is related to the temporal coverage of occultation. In MY35 occultation measurements occurred during the Ls=0°-10° timeframe, but in MY36 they occurred between 20 and 30° at a time when the atmosphere is becoming warmer (Fig. 6A). The second supersaturated area is located at low-to-mid latitudes. There, the lowest supersaturated altitude is found around 40 km near the equator and at 55-60 km at 40°S and 45°N of latitude. This saturation layer is located above the cloud formation region that is lofted below 40 km. The cloud level marks a sharp decrease in water from 50 ppmv to 3-5 ppm, as a result of condensation.

From equinox to solstice, the ~200 K near-surface temperature maximum shifts to the middle (Ls=30°-60°) and high (Ls=60°-90° and 90°-120°) northern latitudes (Fig. 6A). The water maximum also shifts from 50-80 ppmv below 20 km at latitudes of 20-50°N, with an increase to the pole to 100-200 ppmv below 20 km at 30-70°N (Fig. 6B). In these areas, water is always far from saturation. In the Southern Hemisphere, at Ls=30°-60°, 30-50 ppmv of water is still observed near the surface in the mid-latitudes. At higher altitude (~40 km) of the high latitudes, a drier layer of water of about 3 ppmv persists and is associated with large supersaturation above 50 km where almost no aerosol is observed (Fig.6 C, D). In the southern polar latitudes below 20 km, water also begins to be supersaturated despite the drier sub-ppm conditions 1. At Ls=60-90° and 90-120° from middle southern to middle northern latitudes the water decreases above the cloud region at 35-40 km from 30-50 ppmv to <1-2 ppmv . Once again, water above the cloud level layer is found to be highly supersaturated (Fig. 6 A-C).

Closer to autumn equinox, the Ls=120°-150° and 150°-180° intervals show a shift of the water peak to the equator again, following the onset of the equinoctial circulation pattern, characterized by two cells facing each other around the equator. However, no strong supersaturation was observed below 20 km in the northern polar region due to warmer temperatures compared to the southern polar region.

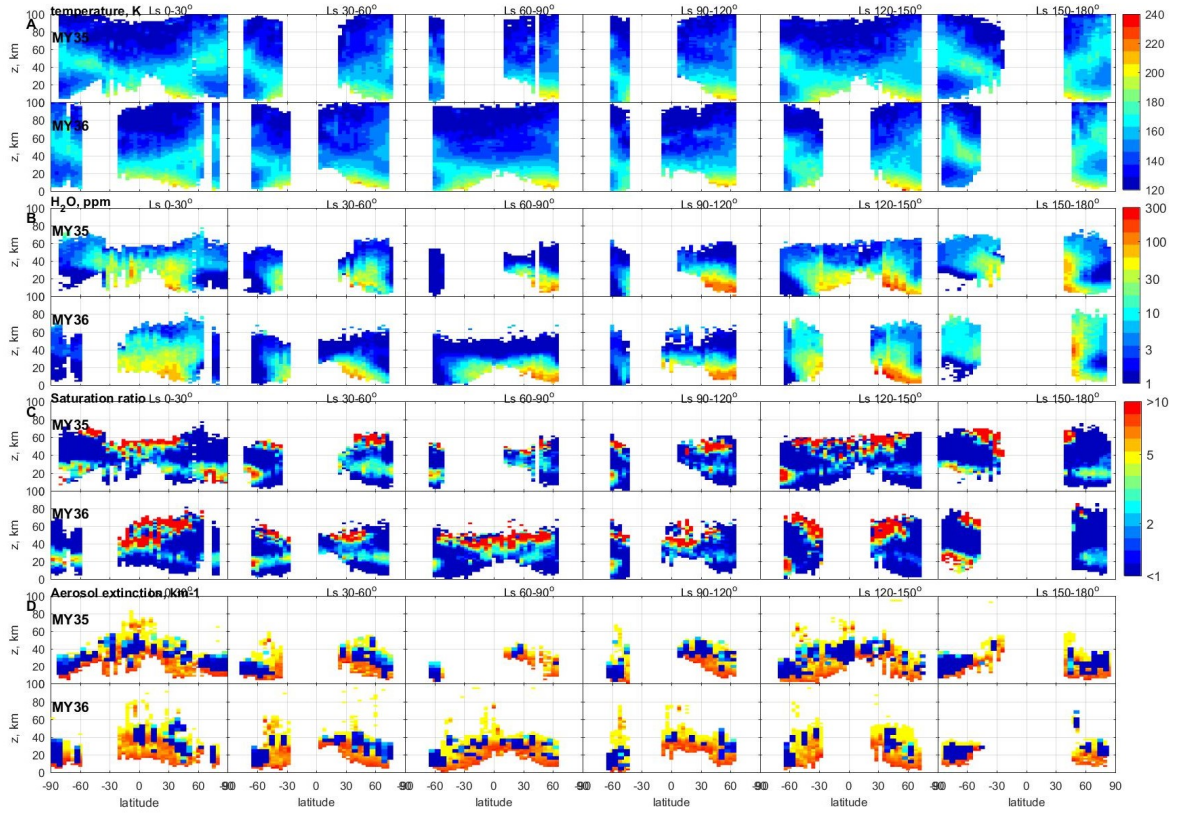

Figure 6. Latitudinal variation of temperature (A), water vapor (B), saturation ratio (C) and aerosol extinction, yellow-red – dust, shades of blue – water ice clouds, (D) vertical profiles in the aphelion season from Ls=0° to 180° for two Martian years MY35 and MY36. The retrievals are binned in 30° of Ls with an interval of 1° of latitude and 2 km of altitude.

3.3 Perihelion season

Figure 7 shows the same latitudinal variations of temperature, water vapor, saturation ratio and aerosol extinction as Figure 6, except for the perihelion season from Ls=180 to 360°, in 30° Ls bins for MY34 and 35.

The Martian year 34 was characterized by the GDS that began at Ls=193° and vanished around Ls=240°. This event generated a strong interannual variability between MY34 and MY35 from Ls 180 to 240°. During MY35, water is distributed from 60°S to 45°N with values of 200 ppmv found in the South up to 60 km, above which water decreases down to 30 ppmv at 80 km. In the North, these high abundances are only seen up to 40 km. The atmospheric layer where most of the decrease occurs is well correlated with aerosol extinction and temperature. This period of time corresponded to the onset of large supersaturations.

Close to the poles, the 10 to 30 ppmv water layers located at 40-70 km appear correlated with warm temperatures and are likely the result of advection. Below 40 km, temperatures decrease, and water falls to <1 ppm, still exhibiting some slight supersaturation. As reported by other studies (Neary et al., 2020, Heavens et al.), the MY34 GDS warmed the atmosphere as captured by ACS in the North (Fig. 7A) where the temperature below 60 km is 30-40 K warmer than in MY35. In the southern hemisphere the region between 10°S-60°S was observed before the GDS whereas the region between 60°S-90°S could only be observed after it started (Fig. 3). This period is characterized by water observed up to 80 km with values of 200 ppmv, which sharply decrease to 30-50 ppmv above 100 km (Belyaev et al., 2021). At this season, water begins to be supersaturated only above 70-80 km where clouds actually form (Fedorova et al., 2020; Luginin et al., 2020). At Ls=210°-240° the atmosphere is much warmer than in MY35. Water mixing ratios up to 100 ppmv were observed at high altitudes, that is above 70 km in high southern latitudes and above 60 km in high northern latitudes. In both cases, water is again observed to fall rapidly down to a mixing ratio of 30 ppm. At these high altitudes, water is supersaturated, yet aerosols are present up to 100 km, indicating that cloud or aerosol presence was not sufficient to relax the atmosphere to saturation. In MY35 between 45°S-60°N, 100-200 ppmv of water prevails below 40-50 km with a decrease to 5-30 ppmv above. Again, water is strongly supersaturated up to 60 km even in the presence of aerosols. At 70-50°S, the water maximum is pushed higher, up to 80-100 km, which may actually be the consequence of the set-up of the solstitial circulation (Richardson and Wilson, 2002a, 2002b; Montmessin et al., 2007).

During the southern summer solstice Ls=240-270° and 270-300° the water distribution is very similar for two years with an asymmetry between hemispheres also observed by SPICAM/MEx (Fedorova et al., 2021). In the mid-to-high southern latitudes 200 ppmv are observed up to 60-70 km. This water top gradually decreases to 40 km in the northern hemisphere at 60°N. At these altitudes clouds are observed for both years from 60°S to 60°N. At 30-70°S above 70 km the water abundance sharply decreases to 50-70 ppmv and reaches 100 km and higher. In the northern hemisphere H_2O decreases to 10-30 ppmv between 40 and 80 km and then increases again, revealing the transport of water from the southern to the northern hemisphere at high altitudes. Water is strongly supersaturated during this season for both years. But saturation is much higher for MY35 compared to MY34 and begins above 40 km near the equator and above 70 km at high latitudes . Moving to the northern vernal equinox, circulation is shaping a nearly symmetric picture that is observed both years. The regional dust storm "C" happened between Ls=315° and 330°, whose effect can be grasped in the Ls=300-330° interval in the form of a rise of water mixing ratio and aerosol extinctions up to 70-80 km in the 45°S-70°S region. In both years, supersaturation was observed at high altitudes with water mixing ratio about 30 ppmv. At Ls=330-360° in high southern polar latitudes below 20 km the supersaturation reappears despite the sub-ppmv concentration. A simple interpretation points to the local cooling of the polar atmosphere, as water is

still present and condensation is unable to keep up with the fast temperature decrease.

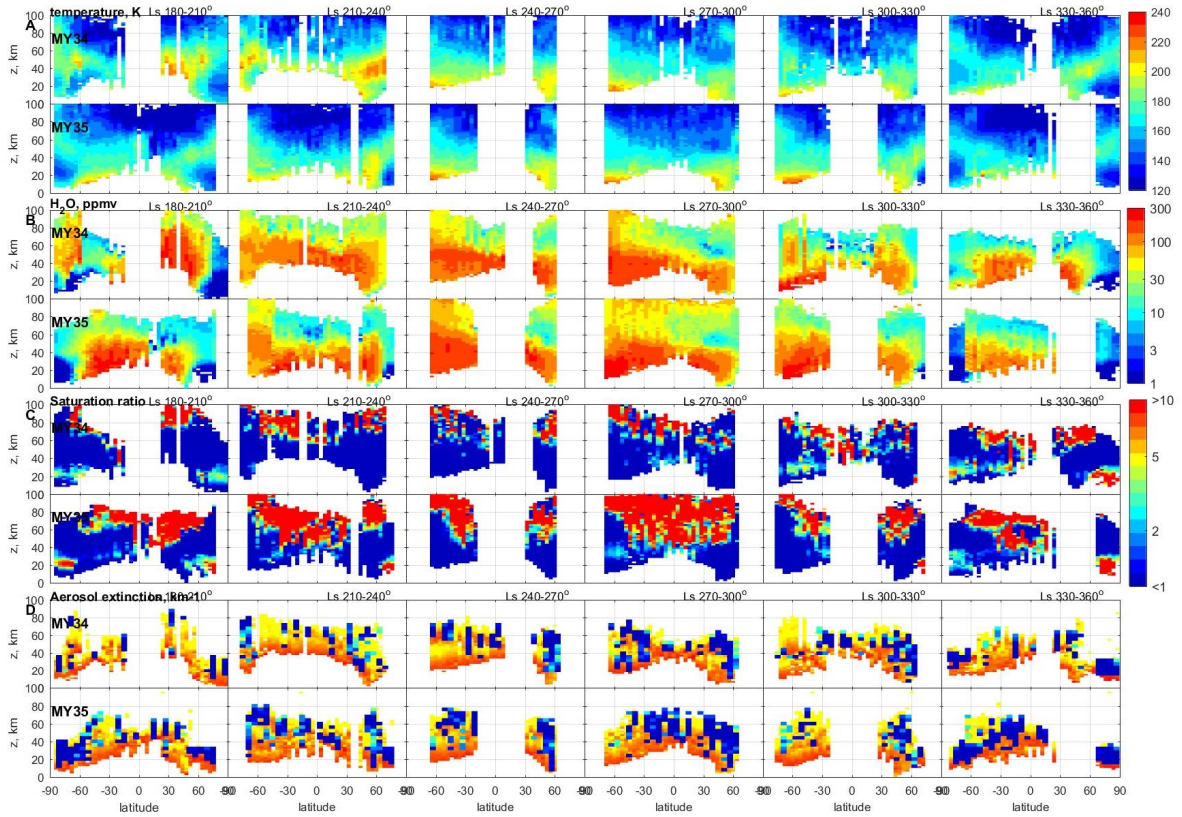

Figure 7. Latitudinal variation of temperature (A), water vapor (B), saturation ratio (C), aerosol extinctions, yellow-red – dust, shades of blue – water ice clouds, (D) vertical profiles in the perihelion season from Ls=180° to 360° for two Martian years MY35 and MY36. The retrievals are binned in 30° of L_s, with an interval of 1 of solar longitude and 2 km of altitude.

3.4 Local time variations.

Diurnal temperature variations in the Martian atmosphere has been observed by many spacecraft such as TES/MGS, MCS/MRO, PFS/MEX and ACS TIRVIM/TGO (Wilson et al., 2000; Heavens et al., 2011; Kleinbohl et al., 2013; Giuranna et al., 2021; Guerlet et al., 2022). These data have allowed the study of thermal tides driven by diurnal solar forcing (Forbes et al., 2020;). Thermal tides dominate the temperature daily cycle over most of the atmospheric column. Along with diurnal tides, semi-diurnal tides dominate the temperature structure of the middle atmosphere throughout the year from high to low latitudes (Kleinböhl et al., 2013). The morning to evening difference

in temperature should therefore also impact water vapor and ice, as they are captured by ACS occultation at both terminators.

The saturation state should also be sensitive to the presence of dust as condensation nuclei in the atmosphere. Observations by PFS have revealed local time variations of dust opacity in the atmosphere. Wolkenberg & Giuranna (2021) have found that aphelion dust opacities are minimum at night and early morning, with perceptible variations during the rest of the day. During the dusty season, no local time variation was found (Giuranna et al., 2021). Diurnal variation of dust was also found during the GDS of MY34 by the Mars Climate Sounder (Kleinböhl et al., 2020) when dust was found at the highest altitudes in the late afternoon and at the lowest altitudes late at night. In addition, dust diurnal cycle was observed to vary with latitude.

The ACS dataset allows us to study the local time variations of water vapor by comparing occultation measurements in the morning and evening terminators. Typically, measurements on the sunset and sunrise belong to different hemispheres, precluding a meaningful comparison of their respective atmospheric state. However, from time to time, a range of close latitudes was probed in the morning and evening terminators within short L_s intervals (Fig. 8). To examine the morning to evening contrasts, we chose seven intervals: two in MY34 (230-250°, 290-310°); four in MY35 (115-135°, 200-220°, 270-290°, 330-350°), and one in MY36 (50-70°). Within each bin, the local time varies along the latitude (see Fig. 8, bottom panels).

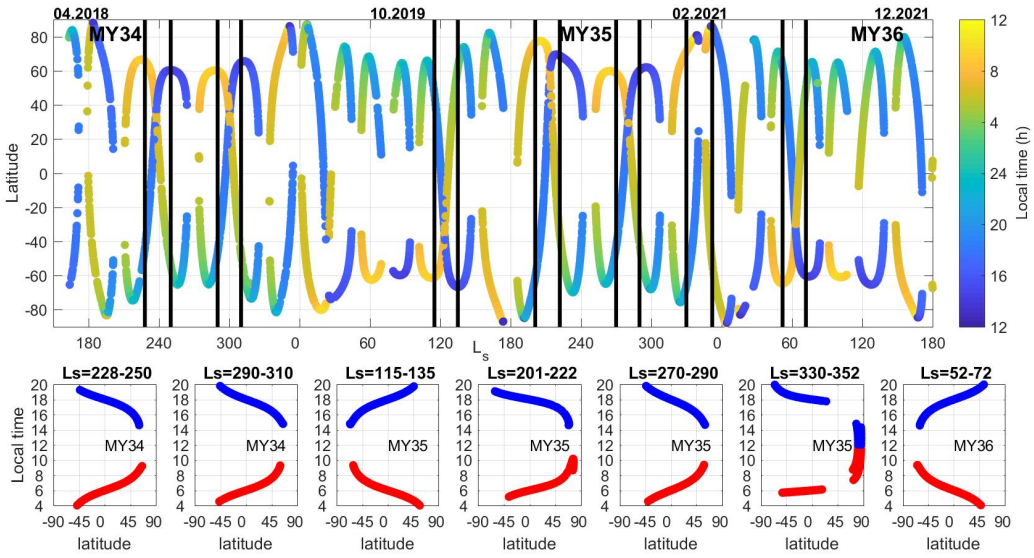

Figure 8. Latitudinal distribution of ACS NIR occultation with ranges selected for search of local time variations (black vertical lines). Bottom panels: zoom at local time inside the indicated bins with red curves for morning terminator

and blue curves for evening terminator.

Figure 9 presents a latitude-altitude cross-section of temperature and water vapor at morning and evening terminators, with the difference between them. A typical signature of thermal tides is prominent in the difference, with negative and positive temperature differences alternating along the vertical and stretching horizontally along latitudes. Two bins around aphelion, one in MY35 after solstice L_s=115°-135° and one in MY36 before solstice, L_s=50°-70°, reveals positive difference at 40 and 80 km and negative difference at 60 km in low latitudes where sampled local times correspond to 06:00AM and 06:00PM (Fig. 8). These patterns are reminiscent of MCS/MRO observations (Kleinböhl et al., 2013) and ACS TIRVIM/TGO (Guerlet et al., 2022). At 45°S and 45°N, there is a flip of sign in the temperature difference. There, the temperature difference exceeds 20 K. During these seasonal bins, water vapor mixing ratios were below 3-5 ppmv between 40-60 km, and from 10 to 200 ppmv below 40 km at low-to-mid latitudes. Despite the warm temperature anomaly observed at the morning terminator at 60 km in the equatorial region, water is located mostly below. At 40 km, the temperature was warmer in the evening by 20-25 K , and we observed more saturation in the morning. In the lower atmosphere more water was observed in the evening below 30 km in the middle northern latitude where 5-10K warmer temperatures were measured.

During the dusty season (at L_s=200°-220° and 270°-290° of MY35) the evening temperature was warmer by 20-30 K from 30°S to 30°N at altitudes ranging from 40 to 65 km. This maximum is correlated with low saturation ratio in the evening (~1-2) compared to strong supersaturation in the morning. Water distribution also varies with local time. At L_s=200°-220°, water abundance increases by 10-40 ppmv in the evening at all altitudes. From Ls 270° to 290°, more water is observed in the evening between the equator and 45°S. This morning-to-evening increase might be attributed to an intensification of the mean upward motion during daytime. A similar configuration has also been seen during L_s 230° to 250° of MY35 before solstice.

Close to the northern vernal equinox (330°-350°) of MY35 the warmer temperature prevailing from 40 to 60 km in the low-to-mid southern latitudes in the evening also raises the saturation altitude by 20 km compared to the morning, with water vapor mixing ratio being higher by 10-30 ppmv compared to the morning.

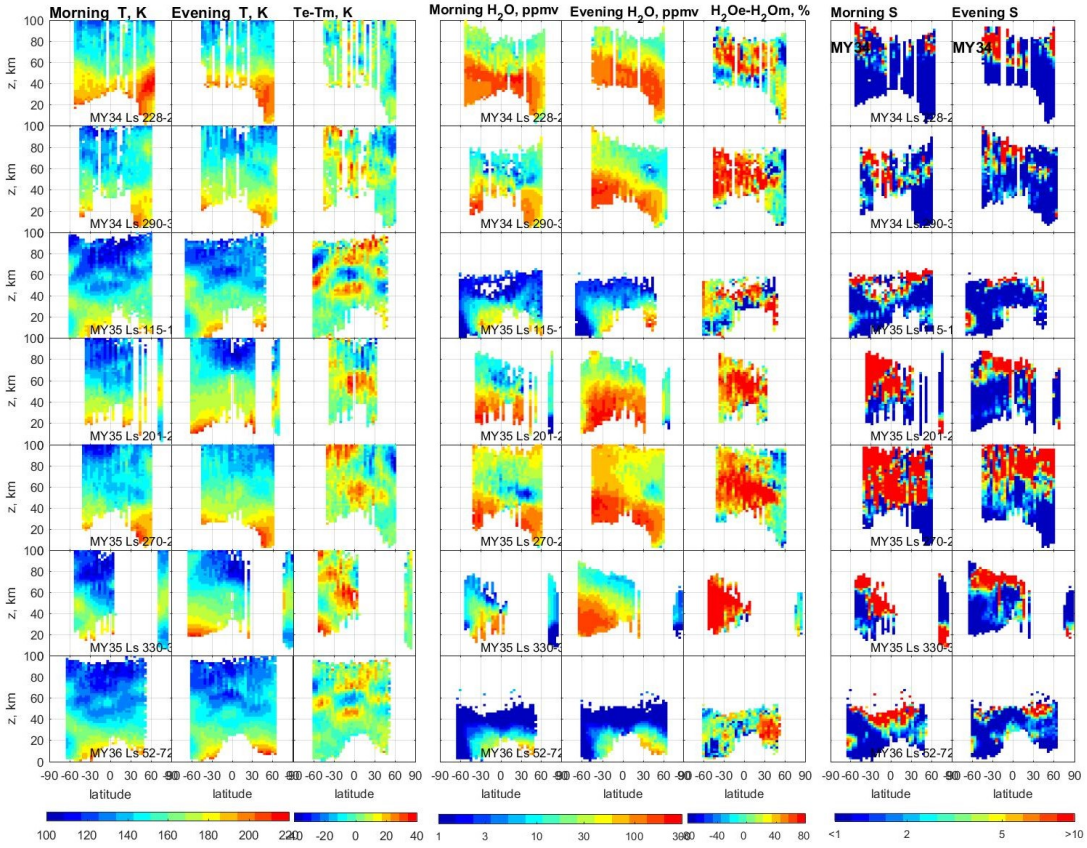

Figure 9. Morning to evening temperature contrast, water vapor and saturation ratio vertical profiles in the selected seasonal bins, from top to bottom: MY34, Ls=230°-250°, 290°-310°; MY35: Ls=115°-135°, 200°-220°, 270°-290°, 330°-350°; MY36: Ls=50°-70°. From left to right: morning, evening, and differences in temperature in K (left), water vapor mixing ratio in ppmv and difference in percents (center), morning and evening saturation ratio S (right).

4. Discussion.

The first evidence of water supersaturation in the Martian atmosphere was obtained during the aphelion season (from L_s 50° to 120°) by SPICAM solar occultations in MY29, when 61 water vapor vertical profiles were retrieved and reported by (Maltagliati et al., 2011). Lacking simultaneous temperature measurements, SPICAM saturation ratios relied on temperature nearly simultaneous MCS/MRO profiles, with a GCM-based correction applied to compensate for the difference in local time between the two instruments. Sixty percent of the data showed water vapor exceeding saturation and more than 10% the saturation ratios greater than 5. Later (Clancy et al., 2017) derived a proxy of water profiles by scaling LMD GCM simulated water vapor by the ratio of LMD

simulated to CRISM retrieved 1.27 m $O_2(^1{}_g)$ dayglow vertical emission rate. Using GCM simulated temperature, the saturation ratio was then averaged during the L_s60° to 140° period. They obtained saturation ratios >2.2 at northern mid-to-high latitudes between 20 and 35 km, which is roughly consistent with SPICAM supersaturation measurements in Maltagliati et al. (2011).

Figure 10 presents the comparison of SPICAM IR observations of water vapor and saturation ratio at Ls=75°-100° with ACS NIR observations in MY35 and 36. Latitudinal coverage of SPICAM and ACS NIR is shown in Fig.10A. In MY34 ACS NIR performed measurements at the same latitudes as SPICAM between Ls=80° and 94°, whereas in MY35 the observations are closer before Ls=83° and after Ls=92°. Despite the coarser vertical resolution of SPICAM IR (1-10 km for SPICAM and <1 km for NIR) and a lower SNR (~100 for SPICAM and ~1000 for NIR), the water vapor vertical profiles of SPICAM (fig.10B) are consistent with NIR profiles in both hemispheres. The increase of water to 100 ppmv below 30-40 km in the northern hemisphere repeats in all years with some temporal and spatial variations. Both SPICAM and ACS NIR have shown the increase of the saturation ratio above 30-40 km where the water v.m.r. sharply decreases to a few ppms. A strong high-latitude supersaturation detected by NIR in the southern hemisphere below 20 km (MY34-35) is supported by SPICAM in MY29 at Ls~80° where latitudes ~60°S were observed. Concluding, SPICAM and ACS NIR observations of H_2O saturation state are generally in good agreement.

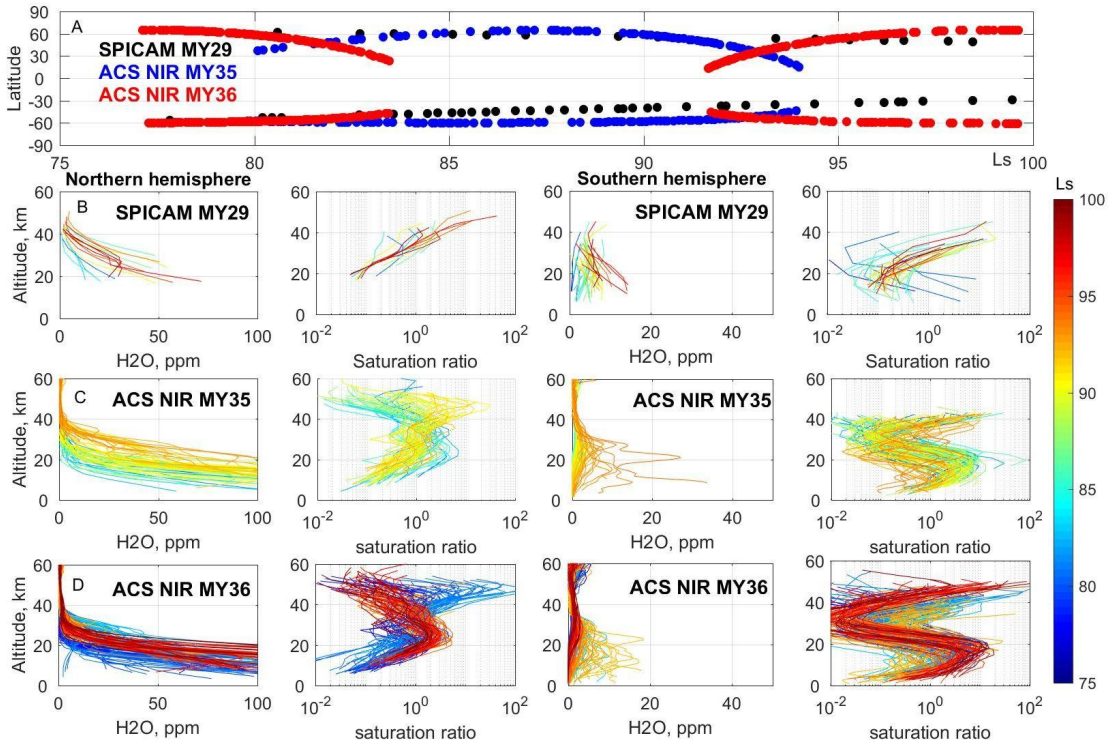

Figure 10. Water vapor vertical profiles and saturation ratio obtained by SPICAM IR occultations in MY29 (B) and ACS NIR observations in MY35 (C) and MY36 (D) at Ls=75°-100° in northern and southern hemispheres. Panel A presents the latitudinal coverage of occultations.

On the contrary, Poncin et al. (2022) did not find evidence for large or widespread supersaturation in the Martian atmosphere. From CRISM analysis they conclude that during the aphelion season the atmospheric water is close to saturation when clouds are present and can reach the supersaturation ratio of 2 to 3 at most at 10–50 km. During the dusty season subsaturation was prevalent, in agreement with previous CRISM study by Clancy et al. (2017). Also, comparison of NOMAD water profiles and MCS atmospheric temperatures during the GDS decay and the "C" storm of MY34 has shown one case of saturation ratio reaching 5 at the top of the cloud layer and below 2 in other cases. These results were more in line with traditional understanding that water vapor is close to saturation in presence of water ice clouds. However, the analyzed water-temperature combinations from CRISM-MCS or NOMAD-MCS datasets were not completely simultaneous. Also, results of Poncin et al. (2022) and ACS TGO do not exclude each other. As shown in Figure 10, the water

vapor mixing ratio and its saturation state are very dynamic and change dramatically from occultation to occultation with latitude and Ls not only in the dusty season presented in Fedorova et al. (2020) but in the aphelion season as well. Solar occultation observations at terminator may reflect both the morning and evening conditions where a strong temperature contrast can stimulate fast processes. Connour et al. (2020) have reported twilight cloud bands routinely forming past the evening terminator (18:00–19:00 local time) during the MY 34 GDS as a result of rapidly changing temperatures. The cloud bands in the IUVS/MAVEN images were often latitudinally continuous, spanning over 6,000 km, and reaching 40–50 km altitudes. Such clouds were also detected in the ACS observations during GDS (Fedorova et al., 2020; Luginin et al., 2020), together with strong lifting of supersaturated water. The morning-to-evening difference of the saturation state observed by ACS (Fig. 9) supports that supersaturation cases can be related to semidiurnal thermal tides in the atmosphere.

The recent study of the MY34 GDS with Mars Assimilated Remote Soundings (OpenMars) dataset of Mars GCM group in the Open University (Holmes et al., 2021a) has shown that discrete layers of supersaturation above 60 km exist across all latitudes during the MY34 dusty season with diurnal variation in the saturation state of the atmosphere. This is consistent with ACS NIR observations not only for MY34 but also for MY35. General consistency of the assimilation and observations gives promising perspective of the water vapor saturation modeling.

6. Conclusions

We analyzed two Martian years dataset of H_2O profiles consisting of solar occultation observations by ACS NIR. The data have been collected from April 2018 (Ls=163° of MY 34) to January 2022 (Ls=170° of MY 36) and contain about 8500 water vertical profiles with simultaneous retrieval of CO_2 density and temperature. The latter was obtained from 1.43 m and 1.65 m CO_2 bands (orders 49 and 54 of the spectrometer) in the range of altitudes from 0 to 110 km and the H_2O mixing ratio in the 1.38 m water band (order 56 of the spectrometer) in the range of altitudes from 0 to 100 km. To provide the comparison with aerosol loading, we used the aerosol extinction at 1.4 µm from the same ACS NIR observations and H_2O ice extinction from simultaneous ACS MIR observation at 3.3 µm H_2O ice band.

With this dataset, we have presented the first detailed analysis of the vertical distribution of water vapor saturation state. Based on a two Martian years dataset, we studied the seasonal, latitudinal and local time variations and found the following:

1. We confirm previous observations (Fedorova et al., 2021) that water vertical distribution is variable with season and reaches 100 km in perihelion and 60 km in the aphelion season. The simultaneous measurement of atmospheric temperature allows us to calculate the saturation state of

water vapor and the supersaturation was found nearly ubiquitous above aerosol layers. This finding implies that water escape processes rely on complex interactions between thermodynamics, dynamics, chemistry and microphysics that only fully coupled climate models can address.

2. In the aphelion season, water mixing ratio above 40 km in the mid-to-high latitudes is observed to be lower than 3 ppmv and is found to be supersaturated in low-to-mid latitudes from Ls=0° to 180°. Also supersaturation was found in southern and northern polar regions below 20-30 km close to both equinoxes, correlating the region where water vapor transported from low latitudes meet cold polar vortex.

3. Around perihelion, water is also supersaturated with a mixing ratio of 30-50 ppmv that is typical of altitudes above 60 km. Stronger saturation is observed during the dusty season in MY35 compared to what was observed in MY34 during the Global Dust Storm and around perihelion. In the dusty season the polar maximum of supersaturation at 20 km is presented in both hemispheres and the most prominent close to equinoxes.

4. Water vapor abundance and its saturation state was found to vary between evening and morning terminators in response to temperature modulation imparted by thermal tides. Although water vapor is found to be more abundant in the evening, colder temperatures observed in the morning induce a daily peak of saturation.

5. The observations at Ls=50°-120° during the aphelion season of MY34 and MY35 have shown a good consistency with SPICAM IR observations on Mars-Express in MY29 that demonstrates that supersaturation is repeatable state of water vapor in the Martian atmosphere from year to year.

Acknowledgments

The ExoMars mission is a joint mission of the European Space Agency (ESA) and Roscosmos. The ACS experiment is led by the Space Research Institute (IKI) in Moscow, assisted by LATMOS in France. The science operations of ACS are funded by Roscosmos and ESA. Authors affiliated with IKI acknowledge funding from the Ministry of Science and Education of Russia. Authors affiliated with LATMOS acknowledge funding from CNES and Centre National de la Recherche Scientifique (CNRS).

Data availability.

ACS data are available from ESA Planetary Science Archive (PSA) Level 2

https://archives.esac.esa.int/psa/#!Table%20View/ACS=instrument. The H_2O, temperature and saturation coefficient vertical profiles generated from ACS measurements and analyzed in this study are available on ftp://193.232.13.174/ACS_NIR_Results/S_climatology/ for review purposes. Data will be stored after review in the Mendeley repository.

References

Aoki, S., Vandaele, A. C., Daerden, F., Villanueva, G. L., Liuzzi, G., Thomas, I. R., et al. (2019). Water Vapor Vertical Profiles on Mars in Dust Storms Observed by TGO/NOMAD. *Journal of Geophysical Research: Planets*, *124*(12), 3482–3497. https://doi.org/10.1029/2019je006109

Belyaev, D. A., Fedorova, A. A., Trokhimovskiy, A., Alday, J., Montmessin, F., Korablev, O. I., et al. (2021). Revealing a High Water Abundance in the Upper Mesosphere of Mars With ACS Onboard TGO. *grl*, *48*(10), e93411. https://doi.org/10.1029/2021GL093411

Chaffin, M. S., Deighan, J., Schneider, N. M., & Stewart, A. I. F. (2017). Elevated atmospheric escape of atomic hydrogen from Mars induced by high-altitude water. *Nature Geosci*, *10*(3), 174–178. https://doi.org/10.1038/ngeo2887

Chaffin, M. S., Kass, D. M., Aoki, S., Fedorova, A. A., Deighan, J., Connour, K., et al. (2021). Martian water loss to space enhanced by regional dust storms. *Nature Astronomy*, *5*(10), 1036–1042. https://doi.org/10.1038/s41550-021-01425-w

Chaffin, Michael S., Chaufray, J.-Y., Stewart, I., Montmessin, F., Schneider, N. M., & Bertaux, J.-L. (2014). Unexpected variability of Martian hydrogen escape. *Geophysical Research Letters*, *41*(2), 314–320. https://doi.org/10.1002/2013GL058578

Clancy, R. T. (2017). Vertical profiles of Mars 1.27 m O2 dayglow from MRO CRISM limb spectra: seasonal/global behaviors, comparisons to LMD GCM simulations, and a global definition for Mars water vapor profiles. *Icarus*, *293*. https://doi.org/10.1016/j.icarus.2017.04.011

Clancy, R. T., Grossman, A. W., Wolff, M. J., James, P. B., Rudy, D. J., Billawala, Y. N., et al. (1996). Water Vapor Saturation at Low Altitudes around Mars Aphelion: A Key to Mars Climate? *Icarus*, *122*(1), 36–62. http://dx.doi.org/10.1006/icar.1996.0108

Clarke, J. T. (2014). A rapid decrease of the hydrogen corona of Mars. *Geophys. Res. Lett.*, *41*. https://doi.org/10.1002/2014GL061803

Connour, K., Schneider, N. M., Milby, Z., Forget, F., Alhosani, M., Spiga, A., et al. (2020). Mars's twilight cloud band: A new cloud feature seen during the Mars Year 34 global dust storm. *Geophysical Research Letters*, 47, e2019GL084997. https://doi.org/10.1029/2019GL084997

Fedorova, A. A., Korablev, O. I., Bertaux, J. L., Rodin, A. V., Montmessin, F., Belyaev, D. A., & Reberac, A. (2009). Solar infrared occultation observations by SPICAM experiment on Mars-Express: Simultaneous measurements of the vertical distributions of H2O, CO2 and aerosol. *Icarus, 200*(1), 96-117. doi: http://dx.doi.org/10.1016/j.icarus.2008.11.006

Fedorova, A. A., Montmessin, F., Rodin, A. V., Korablev, O. I., Määttänen, A., Maltagliati, L., & Bertaux, J. L. (2014). Evidence for a bimodal size dis-

tribution for the suspended aerosol particles on Mars. *Icarus*, *231*(0), 239–260. http://dx.doi.org/10.1016/j.icarus.2013.12.015

Fedorova, A., Bertaux, J. L., Betsis, D., Montmessin, F., Korablev, O., Maltagliati, L., & Clarke, J. (2018). Water vapor in the middle atmosphere of Mars during the 2007 global dust storm. *Icarus*, *300*, 440–457. https://doi.org/10.1016/j.icarus.2017.09.025

Fedorova, Anna A., Montmessin, F., Korablev, O., Luginin, M., Trokhimovskiy, A., Belyaev, D. A., et al. (2020). Stormy water on Mars: The distribution and saturation of atmospheric water during the dusty season. *Science*, *367*(6475), 297–300. https://doi.org/10.1126/science.aay9522

Fedorova, Anna, Montmessin, F., Korablev, O., Lefèvre, F., Trokhimovskiy, A., & Bertaux, J.-L. (2021). Multi-Annual Monitoring of the Water Vapor Vertical Distribution on Mars by SPICAM on Mars Express. *Journal of Geophysical Research: Planets*, *126*(1), e2020JE006616. https://doi.org/10.1029/2020JE006616

Forbes, J. M., Zhang, X., Forget, F., Millour, E., & Kleinböhl, A. (2020). Solar tides in the middle and upper atmosphere of Mars. *Journal of Geophysical Research: Space Physics*, 125, e2020JA028140. https://doi.org/10.1029/2020JA028140

Gamache, R. R., et al. (1995). "CO2-Broadening of Water-Vapor Lines." Journal of Molecular Spectroscopy 170(1): 131-151.

Giuranna, M., Wolkenberg, P., Grassi, D., Aronica, A., Aoki, S., Scaccabarozzi, D., et al. (2021). The current weather and climate of Mars: 12 years of atmospheric monitoring by the Planetary Fourier Spectrometer on Mars Express. *From Mars Express to Exomars*, *353*, 113406. https://doi.org/10.1016/j.icarus.2019.113406

Goff J. A., and S. Gratch, Low-pressure properties of water from −160 to 212 F, *Transactions of the American Society of Heating and Ventilating Engineers,* 25–164, New York (1946).

Gordon, I. E., Rothman, L. S., Hill, C., Kochanov, R. V., Tan, Y., Bernath, P. F., et al. (2017). The HITRAN2016 molecular spectroscopic database. *J. Quant. Spectrosc. Radiat. Transfer*, *203*, 3–69. https://doi.org/10.1016/j.jqsrt.2017.06.038

Guerlet S., N. Ignatiev, F. Forget, T. Fouchet, P. Vlasov, G. Bergeron, et al., (2022) Thermal Structure and Aerosols in Mars' Atmosphere From TIRVIM/ACS Onboard the ExoMars Trace Gas Orbiter: Validation of the Retrieval Algorithm, Journal of Geophysical Research: Planets, 10.1029/2021JE007062, 127, 2.

Heavens, N. G., Kleinböhl, A., Chaffin, M. S., Halekas, J. S., Kass, D. M., Hayne, P. O., et al. (2018). Hydrogen escape from Mars enhanced

by deep convection in dust storms. *Nature Astronomy*, *2*(2), 126–132. https://doi.org/10.1038/s41550-017-0353-4

Heavens, N. G., McCleese, D. J., Richardson, M. I., Kass, D. M., Kleinböhl, A., and Schofield, J. T. (2011), Structure and dynamics of the Martian lower and middle atmosphere as observed by the Mars Climate Sounder: 2. Implications of the thermal structure and aerosol distributions for the mean meridional circulation, *J. Geophys. Res.*, 116, E01010, doi:10.1029/2010JE003713.

Holmes, J., Lewis, S., Patel, M., Aoki, S., Liuzzi, G., Villanueva, G., Crismani, M., Fedorova, A., Alday, J., Kass, D., Vandaele, A. C., and Korablev, O. (2021a). Global variations in the vertical distribution of water during Mars Year 34 from multiple spacecraft observations, European Planetary Science Congress 2021, online, 13–24 Sep 2021, EPSC2021-368, https://doi.org/10.5194/epsc2021-368, 2021.

Holmes J.A., S.R. Lewis, M.R. Patel, M.S. Chaffin, E.M. Cangi, J. Deighan, N.M. Schneider, S. Aoki, A.A. Fedorova, D.M. Kass, A.C. Vandaele, (2021b). Enhanced water loss from the martian atmosphere during a regional-scale dust storm and implications for long-term water loss, Earth and Planetary Science Letters 571, 117109, https://doi.org/10.1016/j.epsl.2021.117109.

Houben, H., Haberle, R.M., Young, R.E., Zent, A.P., 1997. Modeling the Martian seasonal water cycle. JGRP 102, 9069–9083.

Kass, D. M., Kleinböhl, A., McCleese, D. J., Schofield, J. T., & Smith, M. D. (2016). Interannual similarity in the Martian atmosphere during the dust storm season. *Geophys. Res. Lett., 43*. doi: 10.1002/2016GL068978.

Kleinböhl, A., John Wilson, R., Kass, D., Schofield, J. T., & McCleese, D. J. (2013). The semidiurnal tide in the middle atmosphere of Mars. *Geophysical Research Letters*, *40*(10), 1952–1959. https://doi.org/10.1002/grl.50497

Kleinböhl, A., Spiga, A., Kass, D. M., Shirley, J. H., Millour, E., Montabone, L., & Forget, F. (2020). Diurnal Variations of Dust During the 2018 Global Dust Storm Observed by the Mars Climate Sounder. *Journal of Geophysical Research: Planets*, *125*(1), e2019JE006115. https://doi.org/10.1029/2019JE006115

Korablev, O., Montmessin, F., Trokhimovskiy, A., Fedorova, A. A., Shakun, A. V., Grigoriev, A. V., et al. (2018). The Atmospheric Chemistry Suite (ACS) of Three Spectrometers for the ExoMars 2016 Trace Gas Orbiter. *Space Science Reviews*, *214*(1). https://doi.org/10.1007/s11214-017-0437-6

Krasnopolsky V.A. (2019), Photochemistry of water in the martian thermosphere and its effect on hydrogen escape, Icarus, 321, 62-70, https://doi.org/10.1016/j.icarus.2018.10.033.

List R. J., Smithsonian Institution, *Smithsonian meteorological tables.* (Smithsonian Institution Press, Washington, 1984).

Luginin M., A. Fedorova, N. Ignatiev, A. Trokhimovskiy, A. Shakun, A. Grigoriev, et al. (2020). Properties of water ice and dust particles in the atmosphere of Mars during the 2018 global dust storm as inferred from the Atmospheric Chemistry Suite. *Journal of Geophysical Research: Planets, 125(*11*),* 1–22. https://doi.org/10.1029/2020JE006419

Madeleine, J.-B., Forget, F., Millour, E., Navarro, T., and Spiga, A. (2012), The influence of radiatively active water ice clouds on the Martian climate, *Geophys. Res. Lett.*, 39, L23202, doi:10.1029/2012GL053564.

Maltagliati, L., Montmessin, F., Fedorova, A., Korablev, O., Forget, F., & Bertaux, J.-L. (2011). Evidence of Water Vapor in Excess of Saturation in the Atmosphere of Mars. *Science, 333*, 1868-.

Maltagliati, L., Montmessin, F., Korablev, O., Fedorova, A., Forget, F., Määttänen, A., . . . Bertaux, J. L. (2013). Annual survey of water vapor vertical distribution and water–aerosol coupling in the Martian atmosphere observed by SPICAM/MEx solar occultations. *Icarus, 223*(2), 942-962. doi: http://dx.doi.org/10.1016/j.icarus.2012.12.012.

Montmessin, F., Forget, F., Rannou, P., Cabane, M., & Haberle, R. M. (2004). Origin and role of water ice clouds in the Martian water cycle as inferred from a general circulation model. *Journal of Geophysical Research: Planets*, *109*(E10), E10004. https://doi.org/10.1029/2004je002284

Montmessin, F., Haberle, R.M., Forget, F., Langevin, Y., Clancy, R.T., Bibring, J.-P., 2007. On the origin of perennial water ice at the south pole of Mars: A precession-controlled mechanism? Journal of Geophysical Research (Planets) 112, 8. https://doi.org/10.1029/2007JE002902

Navarro, T., Madeleine, J.-B, Forget, F., Spiga, A., Millour, E., Montmessin, F., and Määttänen, A. (2014), Global climate modeling of the Martian water cycle with improved microphysics and radiatively active water ice clouds, *J. Geophys. Res. Planets*, 119, 1479– 1495, doi:10.1002/2013JE004550.

Neary, L., Daerden, F., Aoki, S., Whiteway, J., Clancy, R. T., Smith, M., et al. (2020). Explanation for the Increase in High-Altitude Water on Mars Observed by NOMAD During the 2018 Global Dust Storm. *Geophysical Research Letters*, *47*(7), e2019GL084354. https://doi.org/10.1029/2019gl084354

Poncin L., Kleinböhl A., Kass D.M., Clancy R.T., Aoki S., Vandaele A.C. (2022), Water vapor saturation and ice cloud occurrence in the atmosphere of Mars, Planetary and Space Science, 212, 105390, https://doi.org/10.1016/j.pss.2021.105390.

Richardson, M.I., Wilson, R.J., 2002. A topographically forced asymmetry in the martian circulation and climate. Nature 416, 298–301.

Richardson, M.I., Wilson, R.J., 2002. Investigation of the nature and stability of the Martian seasonal water cycle with a general circulation model. JGR 107. https://doi.org/10.1029/2001JE001536

Rodgers, C. D. (2000). Inverse methods for atmospheric sounding: Theory and practice. River Edge, NJ: World Scientific.

Shaposhnikov, D. S., Medvedev, A. S., Rodin, A. V. V., & Hartogh, P. (2019). Seasonal water "pump" in the atmosphere of mars: Vertical transport to the thermosphere. *Geophysical Research Letters*, 46, 4161– 4169. https://doi.org/10.1029/2019GL082839

Shaposhnikov, D. S., Medvedev, A. S., Rodin, A. V., Yiğit, E., & Hartogh, P. (2022). Martian dust storms and gravity waves: Disentangling water transport to the upper atmosphere. *Journal of Geophysical Research: Planets*, 127, e2021JE007102. https://doi.org/10.1029/2021JE007102

Stcherbinine, A., Vincendon, M., Montmessin, F., Wolff, M. J., Korablev, O., Fedorova, A., et al. (2020). Martian water ice clouds during the 2018 global dust storm as observed by the ACS mid-infrared channel onboard the Trace Gas Orbiter. *Journal of Geophysical Research: Planets*, 125, e2019JE006300. https://doi.org/10.1029/2019JE006300

Stone S. W., R. V. Yelle, M. Benna, D. Y. Lo, M. K. Elrod, P. R. Mahaffy, Hydrogen escape from Mars is driven by seasonal and dust storm transport of water. Science 370, 824–831 (2020).

Trokhimovskiy, A., Fedorova, A., Korablev, O., Montmessin, F., Bertaux, J.-L., Rodin, A., & Smith, M. D. (2015). Mars' water vapor mapping by the SPICAM IR spectrometer: Five Martian years of observations. *Icarus, 251*, 50-64. doi: http://dx.doi.org/10.1016/j.icarus.2014.10.007.

Trokhimovskiy, A., Korablev, O., Kalinnikov, Y. K., Fedorova, A., Stepanov, A. V., Titov, A. Y., et al. (2015b). Near-infrared echelle-AOTF spectrometer ACS-NIR for the ExoMars Trace Gas Orbiter. In *Infrared Remote Sensing and Instrumentation XXIII* (Vol. 9608, pp. 62–70). SPIE. https://doi.org/10.1117/12.2190369

Wilson, R. J. (2000). Evidence for diurnal period Kelvin waves in the Martian atmosphere from Mars Global Surveyor TES data. *Geophysical Research Letters*, 27(23), 3889– 3892. https://doi.org/10.1029/2000GL012028

Wolkenberg, P., & Giuranna, M. (2021). Daily dust variation from the PFS MEx observations. *From Mars Express to Exomars*, *353*, 113823. https://doi.org/10.1016/j.icarus.2020.113823